Supplementary Information For

Robust Two-Color Physically Unclonable Patterns from Controlled Aggregation of a Single Organic Luminophore

Haiyan Chen,[a] Shaoju Li,[a] Lei Xu,[a] Mingjun Wang,[a] Shayu Li[a]*

[a]Chongqing University, College of Chemistry and Chemical Engineering, Chongqing, 401331, PR China. Email: shayuli@cqu.edu.cn

Materials

1-Pyreneboronic acid, 2,4-Dichloro-6-phenyl-1,3,5-triazine, 4-Hydroxyphenylboronic acid, Tetrakis(triphenylphosphine)palladium were acquired from Titan Technology Co., Ltd. Additional materials comprising poly(methyl methacrylate) (PMMA), polystyrene (PS), poly(vinyl alcohol) (PVA), potassium carbonate, and magnesium sulfate were purchased from Shanghai Aladdin Biochemical Technology Co., Ltd. Dichloromethane (DCM) and absolute ethanol were obtained from Chengdu Kelong Chemical Co., Ltd. and purified prior to utilization. Tetrahydrofuran (THF, HPLC grade) was sourced from Alfa-Aesar.

Equipments

The UV-visible absorption spectra were documented with a Hitachi U-3010 spectrophotometer. The steady-state fluorescence spectra were acquired utilizing a Hitachi F-7000 spectrometer. Lifetime and quantum efficiency measurements were conducted with an Edinburgh Instruments FLS1000. Morphological characterization of the solid films was performed via Olympus IX71 microscopy. Phase analysis of the solid powder was executed using a PANalytical X'Pert Powder X-ray diffractometer. All macro-scale images were captured with a Sony DSC-RX10M4 camera.

Computational methods

The range-separated hybrid functional wb97x-d3bj was employed for geometry optimization of ground state and excited state.[1] The vertical transition energies from excited state were evaluated by ri-SOS-wPBEPP86 functional on TDDFT optimized geometries.[2] The def2-SVP and def2-TZVPP basis sets along with matching auxiliary sets were used in geometry optimizations and energy calculations, respectively.[3] Tetrahydrofuran (THF) was modeled as the solvent using the conductor-like polarizable continuum model (CPCM).[4] Visualization of the structures was achieved with the Visual Molecular Dynamics software.[5]

Scheme S1. Synthetic route for the preparation of PPTPM
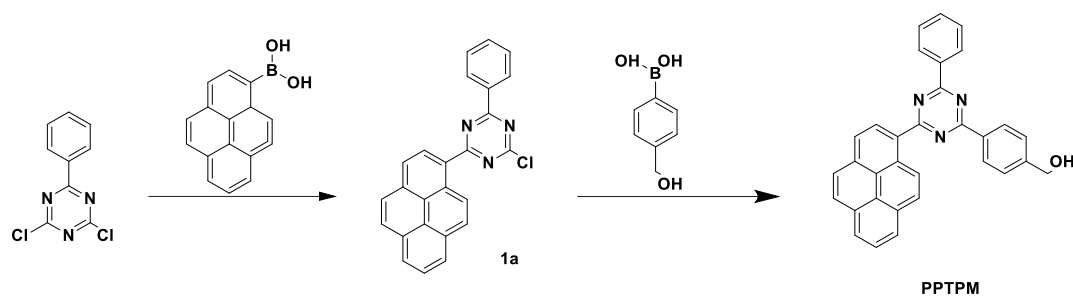
(4-(4-phenyl-6-(pyren-1-yl)-1,3,5-triazin-2-yl)phenyl)methanol (PPTPM): 2-chloro-4-phenyl-6-(pyren-1-yl)-1,3,5-triazine (1a) (0.59g, 1.5mmol, 1eq), 4-hydroxyphenylboric acid (0.25 g, 1.65mmol, 1.1eq), Tetrakis(triphenylphosphine)palladium (0.017g, 5% mmol), potassium carbonate aqueous solution (2 mol/L, 6 ml), ethanol (6 ml) and toluene (12 ml) were placed in a flask, and stirred at 50 ^{0}C under nitrogen protection for 36 h. The resulting solution was diluted with water and extracted with dichloromethane. The organic phase was dried with magnesium sulfate. Purification by chromatography (silica gel, eluent: dichloromethane) provided PPTPM as a cyan-emitting solid (0.41g, 59 %).

¹H NMR (400 MHz, Chloroform-*d*) δ 9.51 (d, *J* = 9.4 Hz, 1H), 9.02 (d, *J* = 8.1 Hz, 2H), 8.84 (td, *J* = 5.1, 2.5 Hz, 4H), 8.34 (d, *J* = 8.1 Hz, 1H), 8.28 (dd, *J* = 8.4, 2.8 Hz, 3H), 8.22 – 8.14 (m, 2H), 8.07 (t, *J* = 7.6 Hz, 1H), 7.66 – 7.58 (m, 5H), 4.86 (s, 2H).
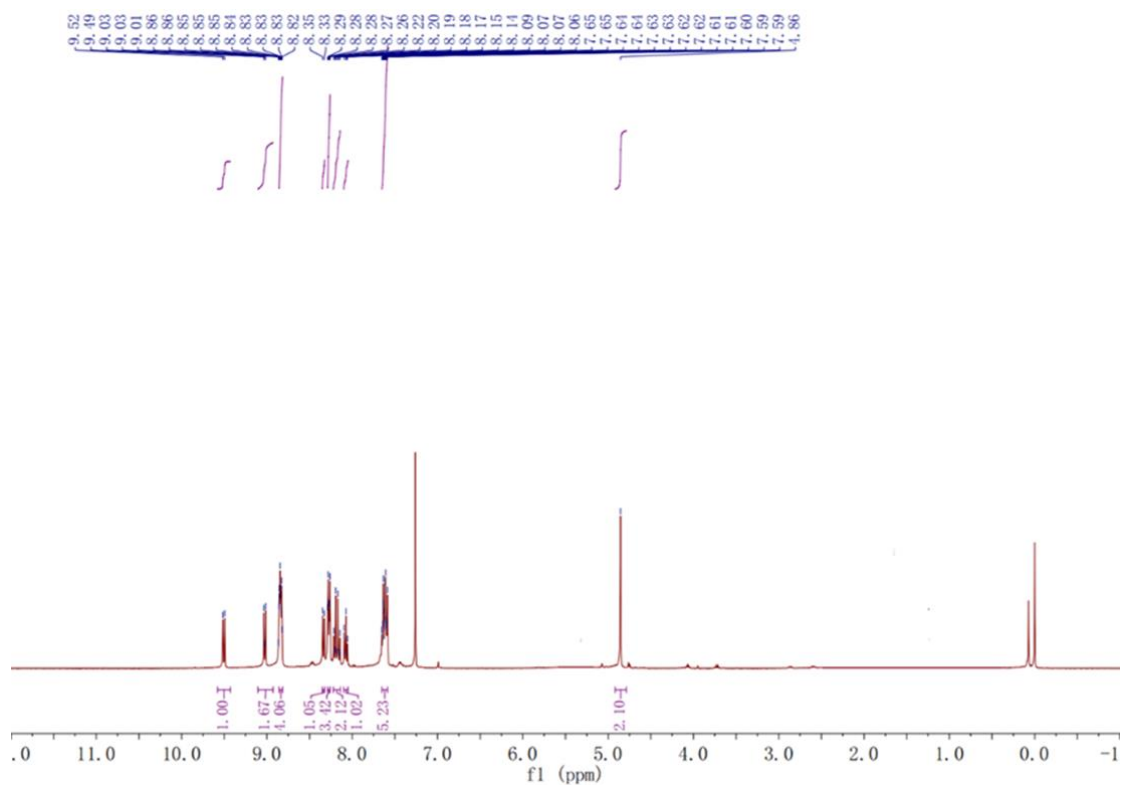

Fig. S1 ¹H NMR (400 MHz, Chloroform-*d*) of PPTPM

¹³C NMR (101 MHz, THF-d8) δ 174.60 , 171.42 (d, J = 8.7 Hz), 148.28 , 136.44 , 134.75 , 132.44 , 131.38 , 130.82 (d, J = 8.5 Hz), 130.48 , 129.38 – 128.39 (m), 127.24 , 126.48 – 124.94 (m), 124.50 , 63.53 .
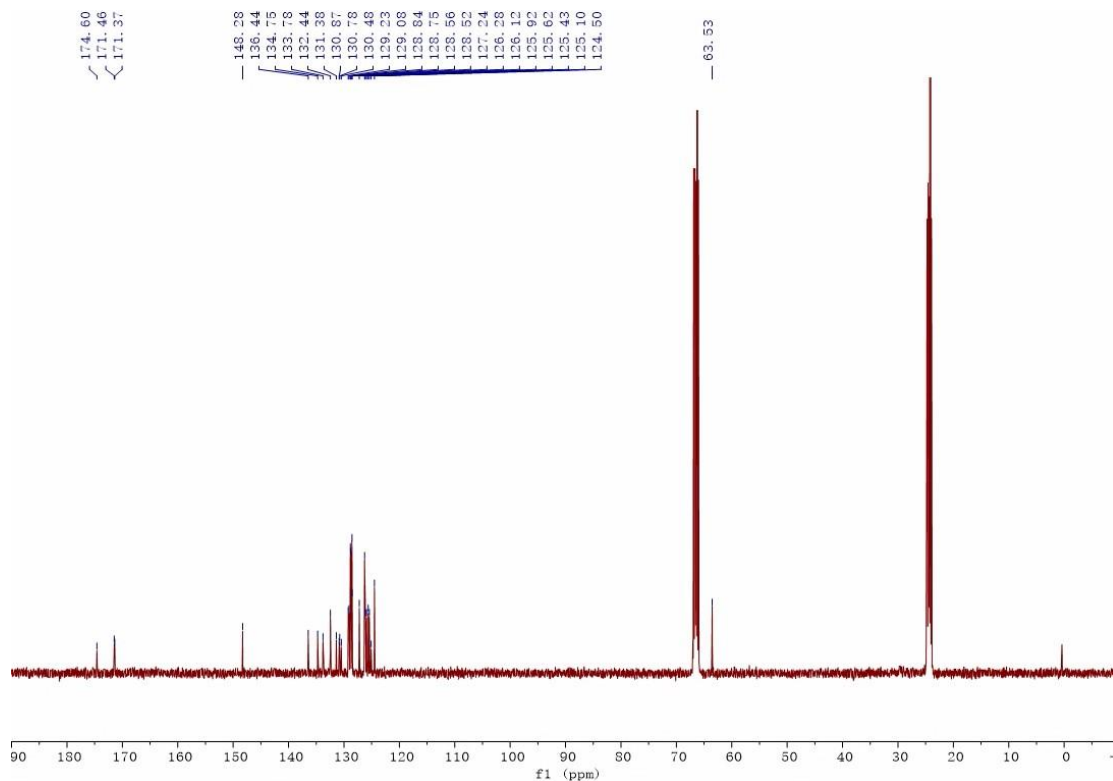

Fig. S2 ¹³C NMR (101 MHz, THF-d8) of PPTPM

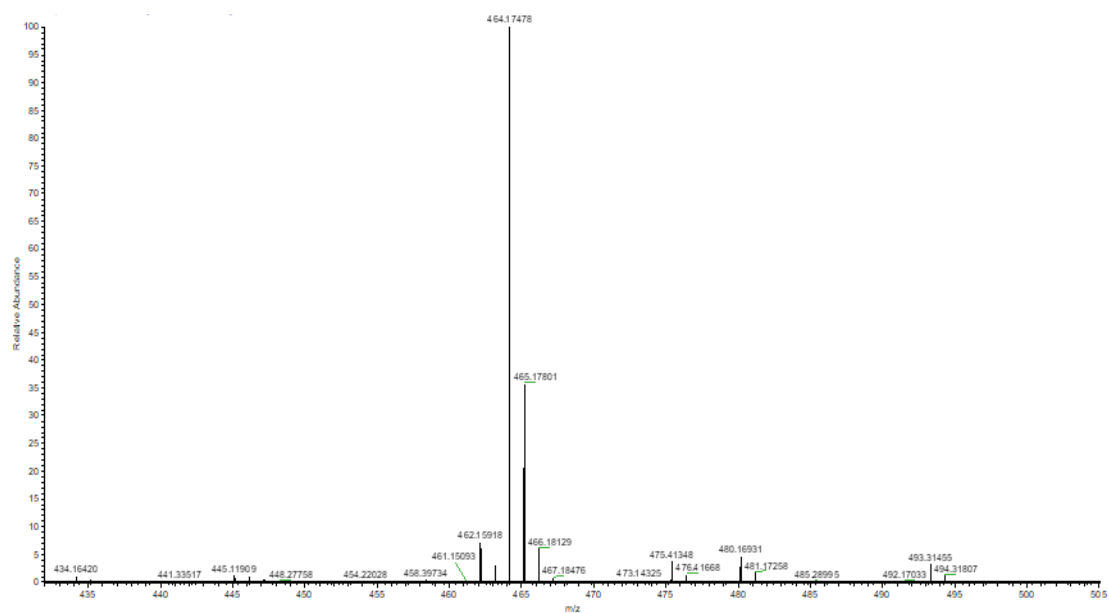**MALDI-TOF [M+H]$^+$ calcd for C$_{32}$H$_{22}$N$_3$O   464.1718; found 464.1748.**

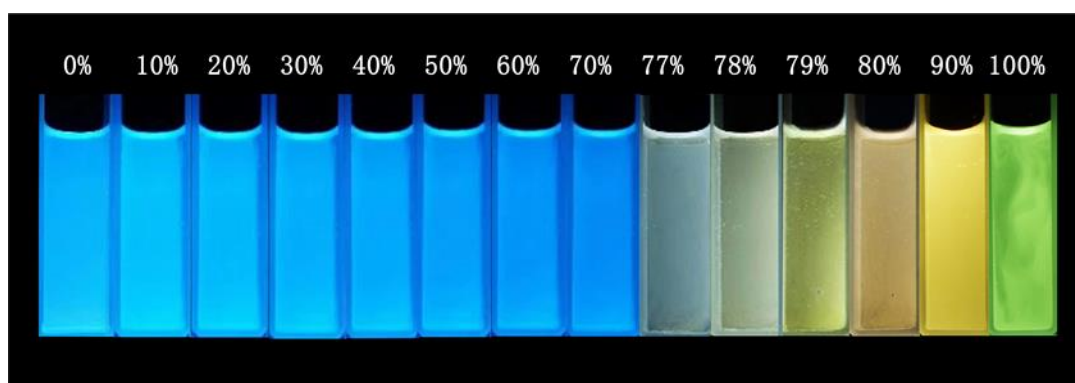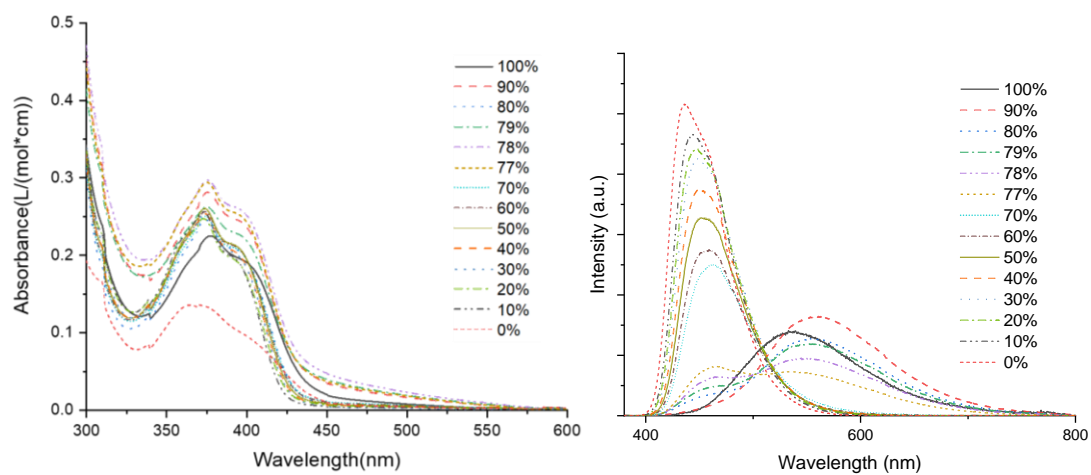**Fig. S3** Mass spectrometry of PPTPM

Fig. S4 Absorption, emission spectra and luminescence image of PPTPM (10μM) in THF/H_2O mixture solutions with different water fractions.
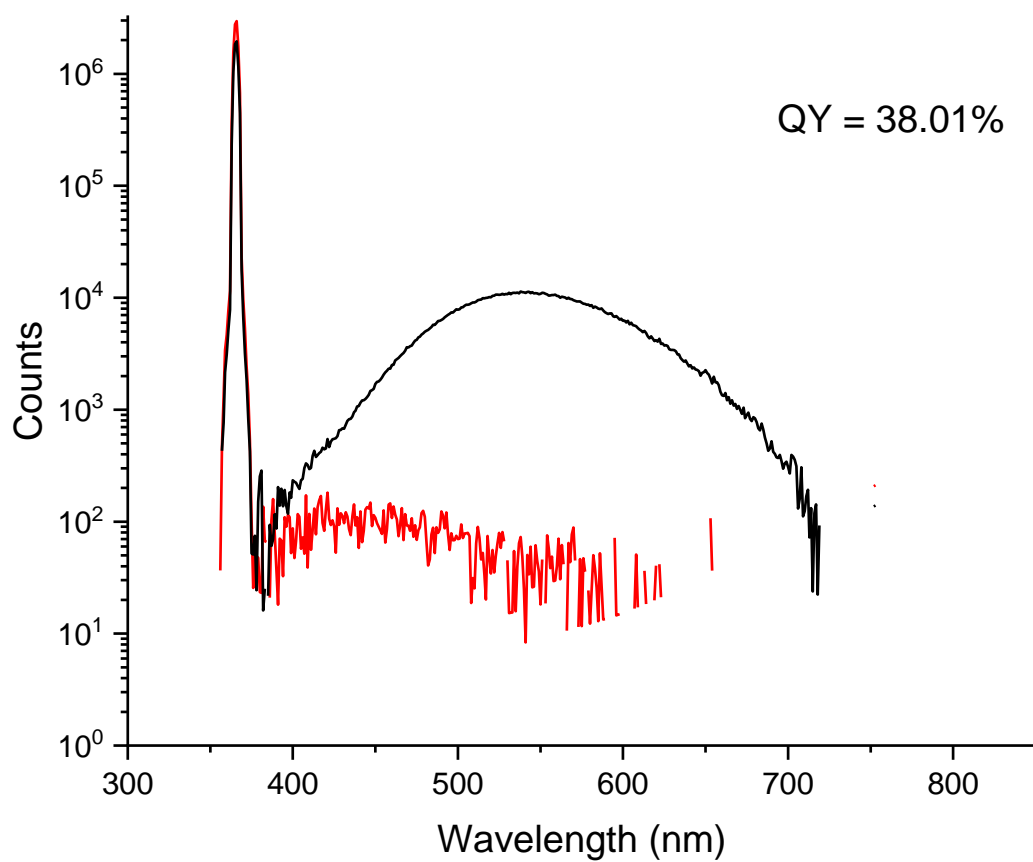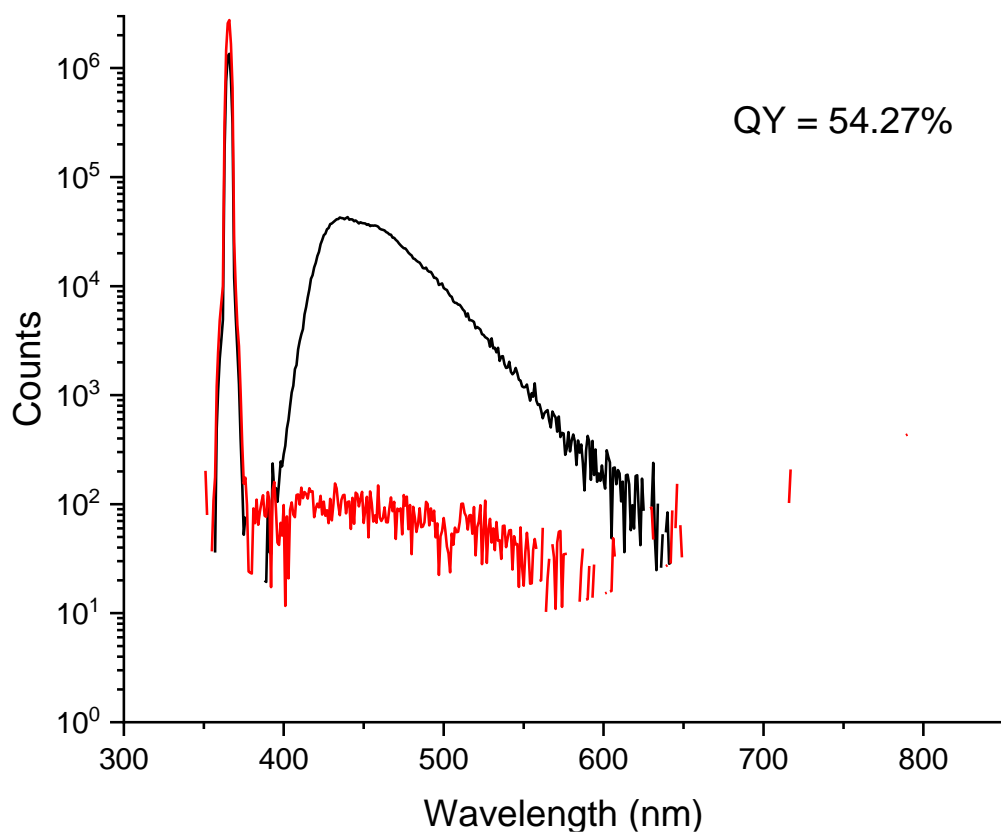
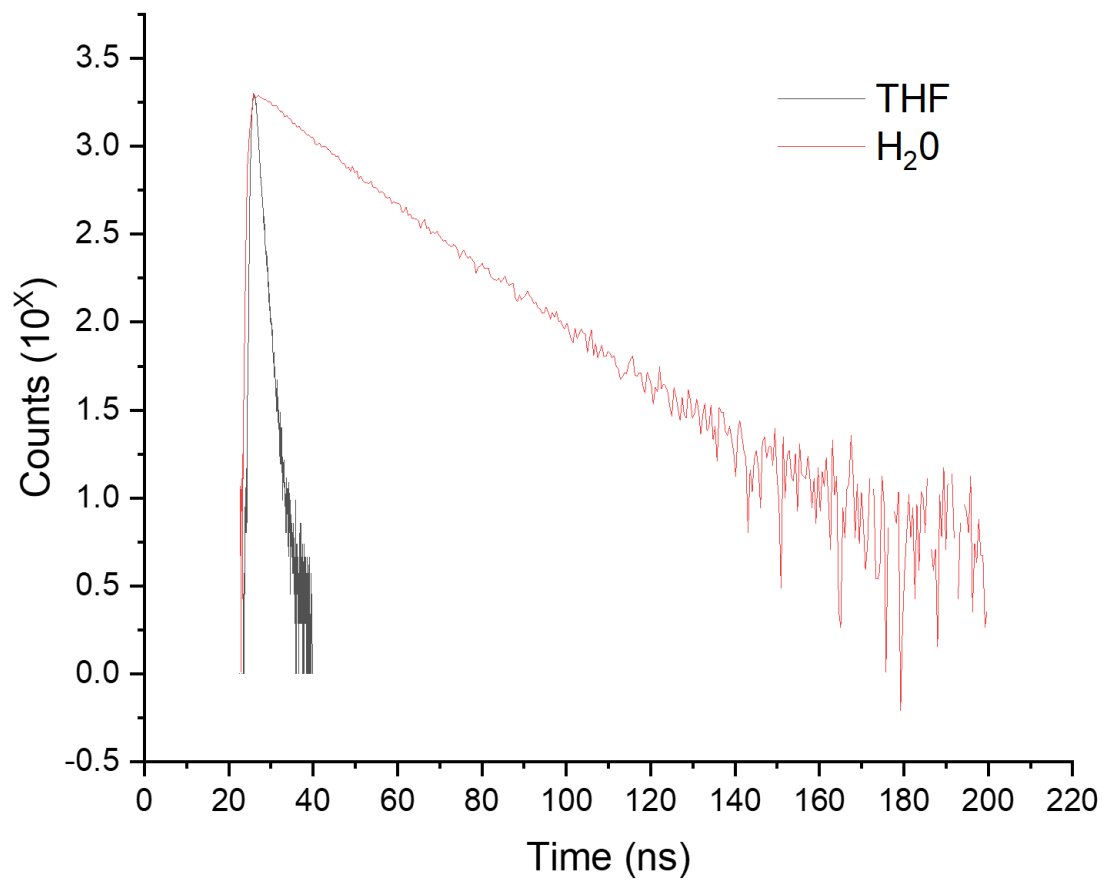**Fig. S5** Quantum yields of PPTPM (10μM) in THF solution and water solution.

Fig. S6 Fluorescence decays of PPTPM (10μM) in THF solution and water solution.

In this study, we have methodically selected four bimolecular configurations to elucidate the diverse interaction scenarios that are representative of our system's complex behavior. Each configuration is designed to highlight distinct aspects of molecular interactions and their photophysical consequences:

Configuration 1: Minimal Electronic Coupling. This configuration involves the pyrene group of one molecule overlapping with the benzyl hydroxyl group of another, deliberately avoiding direct interaction between pyrene moieties. This setup serves as a control, representing scenarios where electronic coupling between the bimolecules is either absent or minimal, thus providing a baseline for comparison with more interactive states.

Configuration 2: Orthogonal Pyrene Coupling. The pyrene groups from two different molecules overlap, yet their long axes are perpendicular. This configuration illustrates suboptimal coupling, indicative of electronic interaction that is geometrically constrained. This particular orientation allows for the investigation of how angular relationships between conjugated planes influence the electronic coupling and, consequently, the photophysical properties.

Configuration 3: Aligned Overlap with Steric Hindrance. In this arrangement, there is a favorable overlap between the pyrene and triazine groups, suggesting potential for strong electronic interactions. However, this ideal overlap is compromised by steric hindrance due to the non-coplanar arrangement of benzyl hydroxyl and pyrene groups. This configuration is crucial for understanding how spatial constraints affect molecular coupling and the resultant photophysical dynamics.

Configuration 4: Ideal Pyrene Interaction. This final configuration represents an ideal case where pyrene groups overlap perfectly, maximizing the potential for strong electronic coupling. Notably, in this scenario, the triazine components do not interact, isolating the effects of the pyrene groups. This model is pivotal for dissecting the pure contributions of pyrene interactions in the absence of other group effects.

These configurations collectively span the range of possible intermolecular interactions, providing a comprehensive framework for understanding how molecular orientation, spatial arrangement, and component interaction collectively influence the photophysical behavior of the system. The insights gained from these studies are instrumental for tailoring molecules for specific applications, such as in advanced anti-counterfeiting technologies, where precise control over photophysical responses is critical.

The close agreement between calculated and experimental emission wavelengths strongly supports the computational model's validity in explaining the observed photophysical behaviors of PPTPM. In isolated solutions, PPTPM molecules emit at the shortest wavelengths observed due to minimal intermolecular interactions. Upon formation of a crystalline solid through controlled drying, molecular proximity significantly increases. This reduced spacing enhances the likelihood of coupling between pyrene groups, which is evident in the cyan luminescence observed in certain configurations.

The calculated values for the hole and electron distributions across different configurations illustrate how molecular packing influences these interactions. Configuration 1, with minimal overlap between pyrene groups, correlates with shorter wavelength emissions closer to the solution-phase spectrum. In contrast, Configurations 3 and 4 show increased pyrene-pyrene overlap, consistent with the red-shifted emissions and broader FWHM noted experimentally. This shift is attributed to enhanced excimer formation, as molecular rearrangements induced by melting and cooling further promote this interaction.

The diversity in luminescent outcomes, highlighted by the broad FWHM and amorphous morphology of the emitting solids, underscores the variability in molecular arrangements. These arrangements range from loosely coupled systems (as in Configuration 2) to highly integrated systems with significant excimer character (as in Configuration 4). It is reasonable to conjecture that actual solid-state luminescence interpolates among these scenarios, providing a spectrum of emission colors based on the degree of molecular packing and alignment.
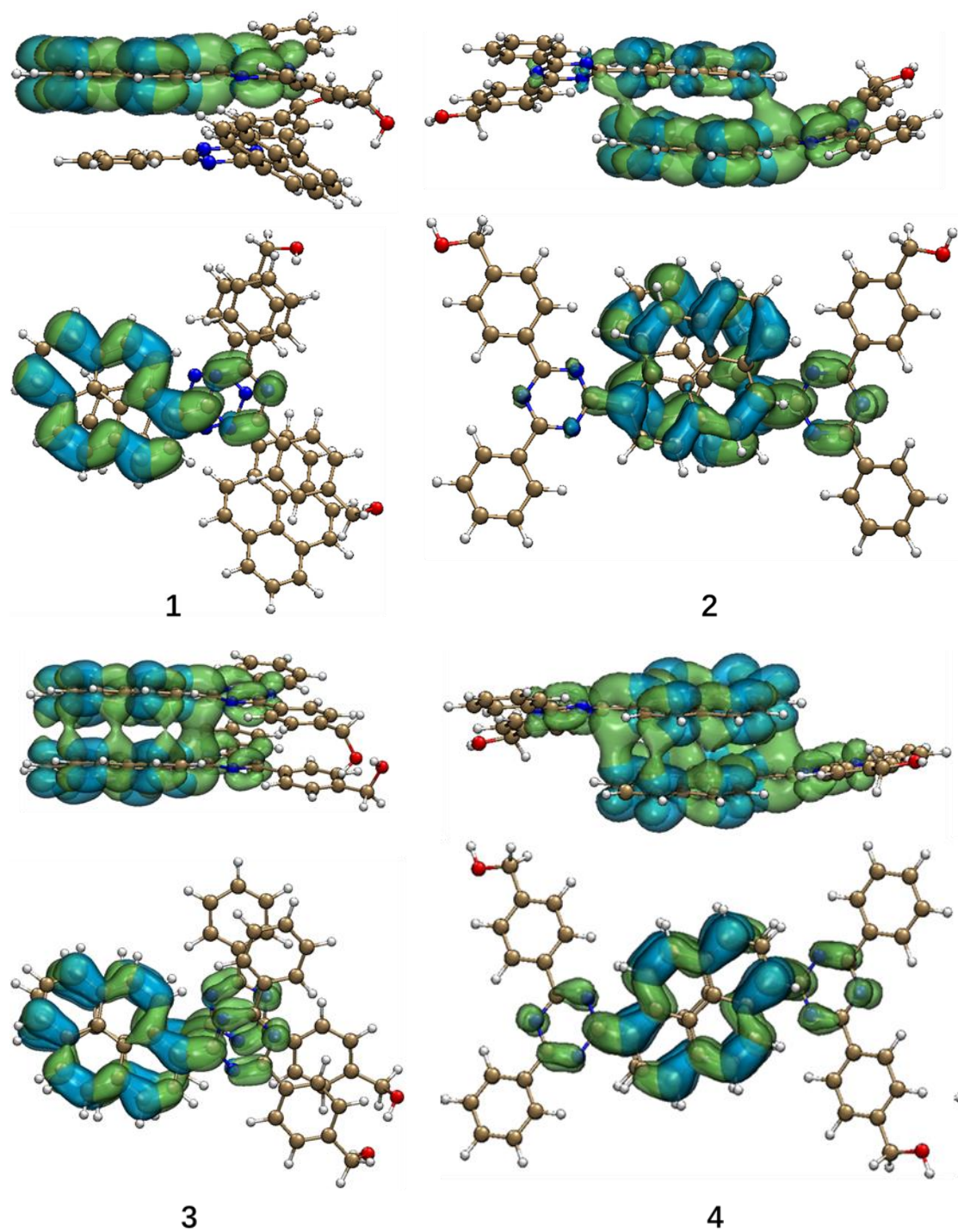
Fig. S7 The hole (blue) and the electron (green) distribution diagrams of four excited state bimolecular configurations.
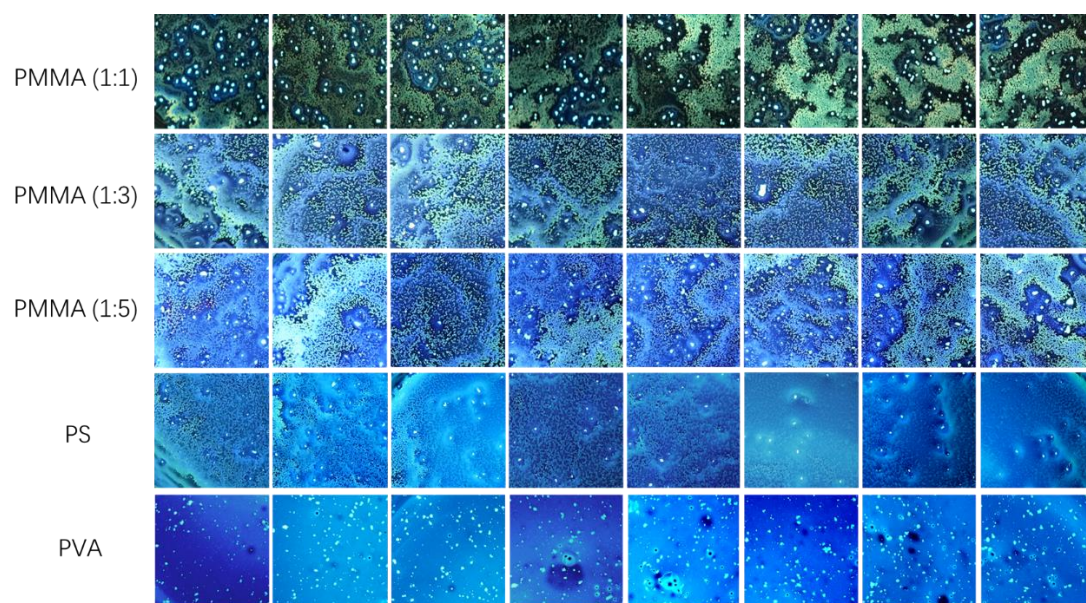
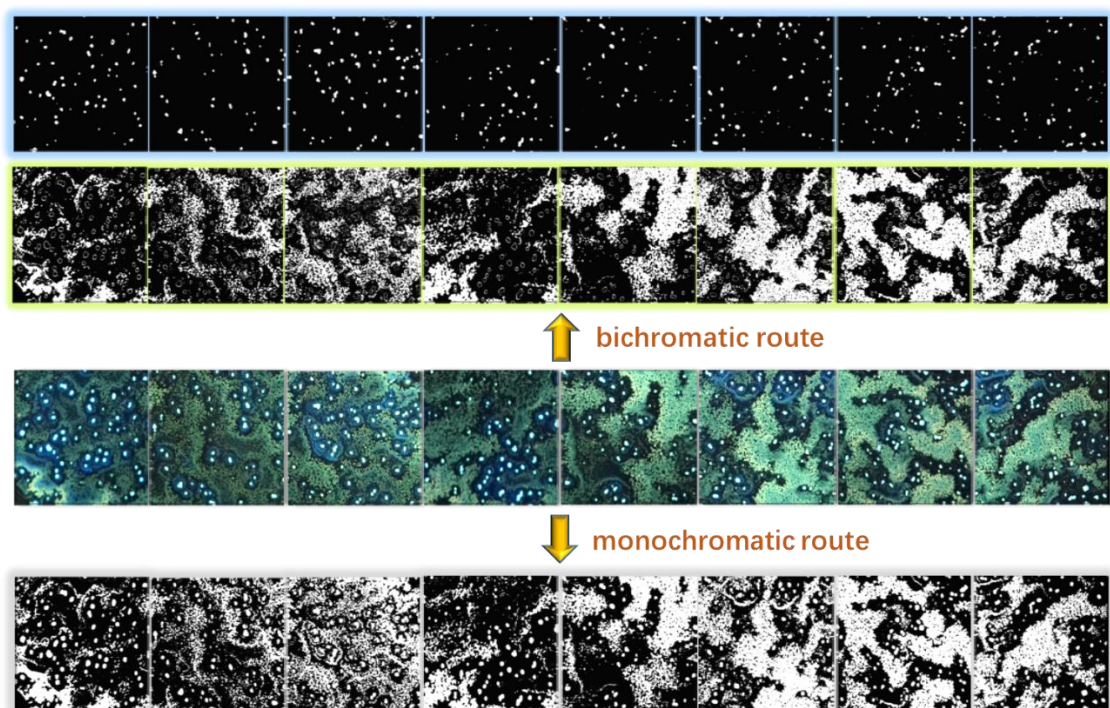**Fig. S8** Photographs of 24 PMMA, 8 PS and 8 PVA PUF labels

Fig. S9 schematic diagram of mono- and bichromatic post-processing routes.

$$\text{Uniformity} = \frac{1}{n}\sum_{i=1}^{n} R_i \qquad (1)$$

where R_i represents the *ith* response (0 or 1) of the n-bit array.

$$\text{Uniqueness} = \frac{2}{N(N-1)}\sum_{i=1}^{N-1}\sum_{j=i+1}^{N}\frac{HD\ (P_i,\ P_j)}{L} \qquad (2)$$

where P_i and P_j representing L-bit sequences from *ith* and *jth* security keys among N different ones, and Hamming distance (*HD*) is the number of different bits at corresponding positions of two equal-length key sequences.

$$\text{Randomness} = 1 - F_{x^2}\left(\sum_{i=1}^{k}\frac{(O_i - E_i)^2}{E_i}; k - 1\right) \qquad (3)$$

where:
- O_i = observed frequency of the *i*-th bit
- E_i = expected frequency of the *i*-th bit
- k = total number of different bit values (here it is 2, representing 0s and 1s)

- $F_{\chi2}(x;k-1)$ = cumulative distribution function of the chi-square distribution with

k−1 degrees of freedom, evaluated at the chi-square statistic x

$$\text{Capacity} = p(1\text{-}p)/\sigma^2 \qquad (4)$$

where p denotes the mean value and σ signifies the standard deviation of the Hamming distance.

$$\text{Reproducibility} = \frac{1}{N}\sum_{t=1}^{N}\frac{HD(P_i, P_{i,t})}{L} \times 100\% \qquad (5)$$

where Pi represents the reference key of the original L-bit, and Pi,t denotes the key extracted from the same PUF label after exposure to environmental factors over time.

Table S1. Performance values for various PUFs

uniformity	0.4395	0.4484	0.6157	0.4089	0.4052	0.4955	0.4984	0.4192	PMMA (1:1)
	0.4141	0.4260	0.5814	0.3894	0.3888	0.4702	0.4762	0.3957	
	0.0254	0.0224	0.0343	0.0195	0.0164	0.0253	0.0222	0.0235	
uniqueness	0.4976 (SD: 0.0179)								
	0.4929 (SD: 0.0165)								
	0.0461 (SD: 0.0059)								
randomness	0.9539	0.9887	0.7471	0.8966	0.8883	0.9494	0.9651	0.9188	
	0.9269	0.9877	0.8582	0.8675	0.9345	0.9316	0.9442	0.8085	
	0.3448	0.3404	0.3549	0.3388	0.3355	0.3451	0.3420	0.3444	
capacity	2^{780}								
	2^{2100}								
uniformity	0.7023	0.6446	0.6542	0.4080	0.2987	0.4338	0.4435	0.4968	PMMA (1:3)
uniqueness	0.5025 (SD:0.0158)								
randomness	0.6858	0.7724	0.7578	0.8540	0.6872	0.8947	0.9100	0.9949	
capacity	2^{999}								
uniformity	0.4823	0.6292	0.4002	0.4051	0.3980	0.4836	0.3828	0.4775	PMMA (1:5)
uniqueness	0.5034 (SD:0.0199)								
randomness	0.9423	0.7299	0.8418	0.9323	0.9372	0.9300	0.9181	0.9426	
capacity	2^{626}								
uniformity	0.7160	0.7900	0.7091	0.5080	0.6813	0.4818	0.4613	0.4356	PS
uniqueness	0.4717 (SD:0.0579)								
randomness	0.6001	0.5008	0.6114	0.8943	0.6469	0.9904	0.9912	0.9011	
capacity	2^{74}								
uniformity	0.0240	0.0480	0.0445	0.0475	0.0798	0.0437	0.0491	0.0612	PVA
uniqueness	0.0911 (SD:0.0181)								
randomness	0.3449	0.3736	0.3686	0.3729	0.4118	0.3676	0.3757	0.3907	
capacity	2^{251}								

Note: Data with grey background are derived from the monochromatic route, while information featuring yellow-green and cyan backdrops originated from the bichromatic route.
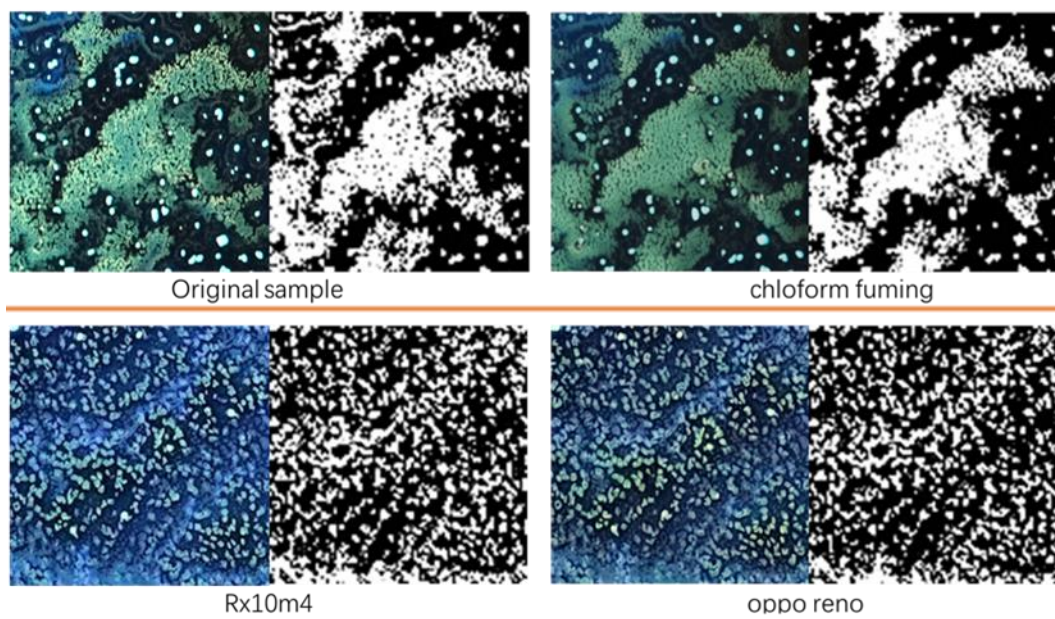
Fig. S10 Stability or reliability evaluations with various solvent fuming and camera devices.

Table S2. The calculated reproducibility values among PMMA PUF labels

PMMA (1:1)			PMMA (1:3)			PMMA (1:5)		
SMPL 1	SMPL 2	Rep.	SMPL 1	SMPL 2	Rep.	SMPL 1	SMPL 2	Rep.
1	2	0.4869	1	2	0.4267	1	2	0.5029
1	3	0.5206	1	3	0.4227	1	3	0.5097
1	4	0.4752	1	4	0.5155	1	4	0.5144
1	5	0.5013	1	5	0.5800	1	5	0.4947
1	6	0.5032	1	6	0.5225	1	6	0.4881
1	7	0.4835	1	7	0.5240	1	7	0.5241
1	8	0.4671	1	8	0.5069	1	8	0.4958
2	3	0.4939	2	3	0.4230	2	3	0.5358
2	4	0.4933	2	4	0.5220	2	4	0.5515
2	5	0.4946	2	5	0.5497	2	5	0.5164
2	6	0.5077	2	6	0.5086	2	6	0.5074
2	7	0.488	2	7	0.5129	2	7	0.5500
2	8	0.4866	2	8	0.5086	2	8	0.5211
3	4	0.5232	3	4	0.5234	3	4	0.4711
3	5	0.5137	3	5	0.5601	3	5	0.4734
3	6	0.5016	3	6	0.5056	3	6	0.4984
3	7	0.4823	3	7	0.5205	3	7	0.4650
3	8	0.5123	3	8	0.5074	3	8	0.4963
4	5	0.4915	4	5	0.4575	4	5	0.4963
4	6	0.4878	4	6	0.4992	4	6	0.4977
4	7	0.4617	4	7	0.5023	4	7	0.4709
4	8	0.5211	4	8	0.5048	4	8	0.5010
5	6	0.5057	5	6	0.4593	5	6	0.4834
5	7	0.5258	5	7	0.4836	5	7	0.4834
5	8	0.5356	5	8	0.5087	5	8	0.4849
6	7	0.4863	6	7	0.4769	6	7	0.4956
6	8	0.4767	6	8	0.4974	6	8	0.4991
7	8	0.5062	7	8	0.4999	7	8	0.4931

References

1 A. Najibi, L. Goerigk, *J. Chem. Theory Comput*. 2018, **14**, 5725-5738.

2 L. Goerigk, S. Grimme, *J. Chem. Theory Comput*. 2021, **17**, 5165-5186.

3 F. Weigend, R. Ahlrichs, *Phys. Chem. Chem. Phys*. 2005, **7**, 3297-3305.

4 V. Barone, M. Cossi, *J. Phys. Chem. A*. 1998, **102**, 1995-2001.

5 W. Humphrey, A. Dalke, K. Schulten, *J. Mol. Graph. Model.* 1996, **14**, 33-38.